processes

MDPI

Article

Experimental Assessment of the Effects of Gas Composition on Volatile Flames of Coal and Biomass Particles in Oxyfuel Combustion Using Multi-Parameter Optical Diagnostics

Tao Li *, Haowen Chen and Benjamin Böhm

Department of Mechanical Engineering, Reactive Flows and Diagnostics, Technical University of Darmstadt, Otto-Berndt Straße 3, 64287 Darmstadt, Germany; haowen.chen@stud.tu-darmstadt.de (H.C.)
* Correspondence: tao.li@rsm.tu-darmstadt.de

Abstract: This experimental study examines the particle-level combustion behavior of high-volatile bituminous coal and walnut shell particles in oxyfuel environments, with a particular focus on the gas-phase ignition characteristics and the structural development of volatile flames. Particles with similar size and shape distributions (a median diameter of about 126 µm and an aspect ratio of around 1.5) are combusted in hot flows generated using lean, flat flames, where the oxygen mole fraction is systematically varied in both CO_2/O_2 and N_2/O_2 atmospheres while maintaining comparable gas temperatures and particle heating rates. The investigation employs a high-speed multi-camera diagnostic system combining laser-induced fluorescence of OH, diffuse backlight-illumination, and Mie scattering to simultaneously measure the particle size, shape, and velocity; the ignition delay time; and the volatile flame dynamics during early-stage volatile combustion. Advanced detection algorithms enable the extraction of these multiple parameters from spatiotemporally synchronized measurements. The results reveal that the ignition delay time decreases with an increasing oxygen mole fraction up to 30 vol%, beyond which point further oxygen enrichment no longer accelerates the ignition, as the process becomes limited by the volatile release rate. In contrast, the reactivity of volatile flames shows continuous enhancement with an increasing oxygen mole fraction, indicating non-premixed flame behavior governed by the diffusion of oxygen toward the particles. The analysis of the flame stand-off distance demonstrates that volatile flames burn closer to the particles at higher oxygen mole fractions, consistent with the expected scaling of O_2 diffusion with its partial pressure. Notably, walnut shell and coal particles exhibit remarkably similar ignition delay times, volatile flame sizes, and OH-LIF intensities. The substitution of N_2 with CO_2 produces minimal differences, suggesting that for 126 µm particles under high-heating-rate conditions, the relatively small variations in the heat capacity and O_2 diffusivity between these diluents have negligible effects on the homogeneous combustion phenomena observed.

Keywords: oxyfuel combustion; coal and biomass; multi-parameter diagnostics; homogeneous ignition; spatial and temporal flame structure

check for updates

Academic Editor: Fabrizio Scala

Received: 6 May 2025
Revised: 26 May 2025
Accepted: 4 June 2025
Published: 8 June 2025

Citation: Li, T.; Chen, H.; Böhm, B. Experimental Assessment of the Effects of Gas Composition on Volatile Flames of Coal and Biomass Particles in Oxyfuel Combustion Using Multi-Parameter Optical Diagnostics. *Processes* **2025**, *13*, 1817. https://doi.org/10.3390/pr13061817

Copyright: © 2025 by the authors. Licensee MDPI, Basel, Switzerland. This article is an open access article distributed under the terms and conditions of the Creative Commons Attribution (CC BY) license (https://creativecommons.org/licenses/by/4.0/).

1. Introduction

Oxyfuel combustion with carbon capture and storage (CCS) offers a transitional solution for reducing the CO_2 emissions from coal-fired power plants while moving toward carbon-neutral electricity production [1]. The utilization of biomass enhances this approach

further by providing an environmentally sustainable alternative that can achieve negative carbon emissions in power generation [2]. However, biomass differs fundamentally from coal in several critical aspects, including its lower heating value, higher moisture content, and more diverse minor constituents. These distinct properties present significant challenges for retrofitting existing coal-fired furnaces, necessitating the careful adaptation of combustion systems to accommodate biomass-specific characteristics [3]. From both fundamental and practical perspectives, homogeneous ignition and early volatile flame development represent critical stages in solid fuel combustion that directly affect flames' stability and propagation dynamics [4]. Advanced modeling approaches have been continuously developed to make better predictions of solid fuel combustion [5], which requires high-quality experimental data for validation. Particle-resolved optical diagnostics have emerged as a powerful tool for elucidating the underlying chemical and physical mechanisms governing these processes [6].

Extensive experimental and numerical progress has been thoroughly reviewed in the literature, with a strong focus on coal combustion [2,7–10] and biomass combustion [2,11–13]. In the literature, the combustion processes for volatile-containing solid fuel particles have been investigated in experiments where the particles are spatially resolved. For high-volatile coal and biomass particles, homogeneous ignition occurs first, releasing volatile matter, such as fuel gases and water, at increasing particle temperatures [14]. Homogeneous ignition and volatile burnout times have been determined using flame emissions [15]. At a high heating rate, homogeneous ignition is the dominant ignition mode, while a transition to heterogeneous ignition occurs as the heating rate decreases [16]. The homogeneous ignition time is influenced by several parameters, including the oxygen mole fractions, particle size, volatile gas composition, particle slip velocity, and the presence of other gases, such as water and CO_2. For instance, it was reported that the ignition delay time increased when N_2 was replaced with CO_2 due to the higher volumetric heat capacity of CO_2 (approximately 1.7 times higher than that of N_2 [17]). Similarly, in O_2/H_2O conditions, ignition is delayed due to the higher heat capacity of H_2O, which is about 1.3 times that of N_2 [18]. However, if the ambient temperature is extremely high, such as the value of 1800 K given in [19], the higher heat capacity of CO_2 leads to a faster devolatilization rate than and a comparable ignition delay time to that in a N_2 atmosphere [20]. Equally, higher O_2 concentrations reduce the ignition delay time [15,21], shorten the combustion duration [22,23], and suppress soot formation [24,25]. When comparing the ignition characteristics across studies from the literature, careful consideration must be given to methodological differences, particularly the sensitivity and resolution of the diagnostic techniques [6,26]. For example, chemiluminescence imaging—while widely used—often lacks the signal sensitivity required for accurate determination of the gas-phase ignition [19]. This limitation can lead to significant variations in the ignition delays reported between studies, even for similar experimental conditions.

Regarding single biomass particles, ignition and combustion were also experimentally investigated at the particle level. Levendis et al. [27] employed flame emission imaging in a drop tube furnace (DTF) to examine the combustion characteristics of coal and sugarcane bagasse. Their observations revealed that biomass produced dimmer, more spherical flames in contrast to the brighter flames typically generated by coal. Khatami et al. [28] investigated the ignition mode and flame temperature of single coal and biomass particles in a drop tube furnace (DTF) using three-color pyrometry. They reported that the volatiles burned simultaneously with the char and formed into a spherical flame, which was closer to the char's surface as the oxygen mole fraction increased. Mock et al. [29] characterized the flame structures of biomass in a jet-in-cross-flow reactor through flame luminosity measurements. Their results indicated that the moisture content affected the ignition delay

time and the volatile flame's brightness, while the duration of volatile combustion was preserved. Simões et al. [30] analyzed biomass combustion in a McKenna burner by using luminosity imaging, showing that the ignition time depended on the gas temperature; however, the oxygen mole fraction imposed an insignificant impact. In addition, extending luminosity to pyrometry techniques, previously reported flame/soot temperature measurements have also distinguished the combustion behavior between coal and biomass particles [31–33]. Recently, our experiments have shown the similar behavior of same-sized coal and biomass particles in terms of their ignition and flame structure evolution [34].

Numerical simulations have significantly advanced our understanding of single-particle ignition and combustion processes [5]. Recent studies have employed diverse computational approaches to investigating these phenomena. Farazi et al. [35] utilized a Euler–Lagrangian framework to analyze gas radical effects in both N_2 and CO_2 environments, while Tufano et al. [36] performed particle-resolved simulations to quantify how gas mixtures influence the ignition characteristics and particle temperature evolution. Different ignition models considering devolatilization and the gas-phase kinetics were evaluated by Goshayeshi et al. [37] and compared against experimental data. A synergistic relationship exists between the numerical and experimental approaches in this field. Optical diagnostics provide critical validation data with well-controlled boundary conditions for simulations, while the computational results offer insights into the experimentally inaccessible parameters in two-phase reactive flows. This complementary relationship is exemplified by our previous studies: experimental swelling ratios were correlated with simulated particle heating rates and assessed in [38], while the experimental ignition/combustion times were combined with simulated radical and temperature data to elucidate the effects of the inert gas composition and oxidizer mole fraction on volatile combustion [19,34].

Our previous work investigated the influence of gas mixtures on the ignition and combustion behavior of coal particles, without considering biomass particles [19]. Subsequently, we extended these experiments to include a comparative analysis of single coal and biomass particles, focusing on differences in the volatile combustion and particle size effects in [34]. However, the roles of oxygen concentration and inert gas composition have not yet been addressed, representing a key gap that the present study aims to fill. Building upon previous work [19,34], this study investigates the single-particle combustion of both biomass and coal in CO_2/O_2 and N_2/O_2 atmospheres, employing advanced optical diagnostics for the simultaneous high-speed measurement of multiple parameters. The primary objective is to systematically evaluate how the gas composition—particularly the oxygen mole fraction and type of inert gas—affects the gas-phase ignition characteristics and structural development of volatile flames. This paper is organized as follows: Section 2 describes the experimental conditions and fuel properties, followed by an overview of the diagnostic techniques and data processing methods. Section 3.1 presents the measurement results for the particle size, shape, and velocity profiles. Section 3.2 analyzes and compares the ignition delay times across different gas atmospheres. Sections 3.3 and 3.4 examine the temporal evolution of the volatile flame structures through a statistical evaluation of high-speed visualization data.

2. The Experimental Methodology

2.1. Combustion Atmospheres and Fuel Particles

Single-particle experiments were conducted using an established laminar flow reactor (LFR), depicted in Figure 1a. The hot flow environment was generated by stabilizing lean, premixed, flat flames on the burner's surface. Solid fuel particles were seeded into the LFR through a 2.9 mm capillary tube via a rotation-wheel dispersion unit. The reactor featured a square-shaped chimney constructed from quartz glass, providing optical access from all

four sides while preventing the entrainment of cold air. This LFR was utilized to study both the single-particle and particle group combustion of solid fuels, and the detailed geometry is given in the previous work [39].

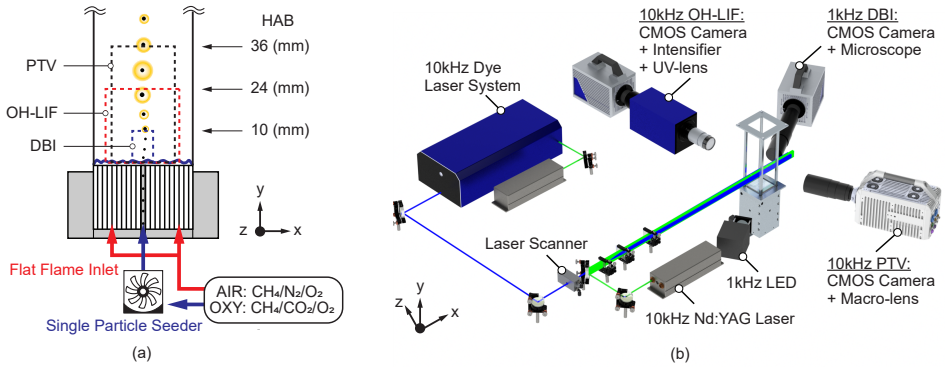


Figure 1. (**a**) A schematic of the laminar flow reactor and the measurement field of view. Different inlet gas mixtures were used in AIR and OXY conditions. (**b**) The optical setup for the multi-parameter measurements [34].

The current investigation utilized seven different operation conditions or atmospheres, as listed in Table 1. These atmospheres were categorized as either AIR or OXY atmospheres, with N_2 or CO_2 serving as the inert gas. The boundary conditions were designed to meet specific requirements: (1) Ensuring that all atmospheres had a similar adiabatic flame temperature T_{ad} and thus similar mean gas temperatures T_m along the center line, as indicated in Table 1. (2) Maintaining comparable gas velocities to ensure a similar conventional heat transfer process. (3) Gradually increasing the volume fraction of oxygen X_{O_2} in the atmosphere (the burned gas of the flat flame). These features of the LFR allowed for a comparison of the conditional parameters and an assessment of the impact of gases, including oxygen and inert gases, on the particle ignition and volatile combustion processes, which was the primary focus of this study. Detailed inlet flow rates for the flat flames and particle jets, respectively, and experimental characterization of the temperature and velocity boundary conditions were reported in [19].

Table 1. The operating conditions of the laminar flow reactor in the post-flame region.

Atmospheres	X_{O_2}	T_{ad} (K)	T_m (K)
AIR10	0.1	1874	1766
AIR20	0.2	1839	1753
AIR30	0.3	1829	1739
AIR40	0.4	1829	1737
OXY20	0.2	1835	1731
OXY30	0.3	1831	1729
OXY40	0.4	1825	1722

One objective of the present experiments is to evaluate the differences in the combustion behavior between single particles of biomass and coal. Specifically, this study focuses on micrometer-sized particles of high-volatile bituminous (hvb) coal and walnut shells, which differ significantly in their elemental and proximate compositions, as shown in Table 2. Walnut shell contains less carbon and more oxygen than coal, indicating the higher reactivity of its volatile species. Its volatile matter (72.93%) content is nearly double that of coal (36.90%), leading to reduced levels of fixed carbon and ash. However, walnut shells also exhibit a significantly higher moisture content—approximately three times greater than that of coal (9.48% vs. 3.50%). These compositional differences suggest that the

volatile-phase combustion of walnut shells may be more intense and sustained than that of coal.

Table 2. Ultimate and proximate analyses of investigated fuel particles.

Fuel		Hvb Coal	Walnut Shell
Ultimate analysis (dry by weight)	C	0.7860	0.5132
	H	0.0530	0.0621
	O	0.1370	0.4236
	N	0.0140	0.0011
Proximate analysis (wet)	Fixed carbon	0.5090	0.1693
	Volatiles	0.3690	0.7293
	Moisture	0.0350	0.0948
	Ash	0.0870	0.0066

To ensure a consistent basis for comparison during ignition and early-stage flame evolution, particles with a similar size and shape were selected. The peak aspect ratio ($\beta_{prt,peak} = 1.5$) and the mean circle-equivalent diameter ($\overline{d}_{prt} = 126$ µm) are summarized in Table 3. This selection was made based on the in situ sizing diffuse backlight-illumination (DBI) measurements, which are discussed further in Section 3.1. In this study, the coal and walnut shell particles are denoted as BC and WS, respectively.

Table 3. Investigated solid fuel particles and their properties.

Particles	$\overline{d}_{prt}$ (µm)	$\beta_{prt,peak}$	Conditions
Hvb coal (BC)	126	1.5	AIR
Walnut shell (WS)	126	1.5	AIR, OXY

2.2. Optical Diagnostics

In order to experimentally investigate the ignition process for single particles, it is essential to spatially and temporally resolve multiple process-relevant parameters. Therefore, this study employed multi-dimensional and time-resolved optical diagnostics, involving simultaneous scanning laser-induced fluorescence of hydroxyl radicals (OH-LIF), diffuse backlight-illumination (DBI), and Mie scattering measurements. A schematic layout of the optical diagnostics is illustrated in Figure 1b. In addition, the technical details of the diagnostics and measured parameters used are given in Table 4.

Table 4. Optical diagnostics: measured parameters and technical details.

	Diagnostics		
	DBI	**OH-LIF**	**Mie Scattering**
Parameters	d_{prt} and β_{prt}	t_{ign}, I_{OH}, and r_{PR}	V_{prt}
Light Source	LED (ILA LPS3)	Nd:YVO4 laser (Edgewave IS8II) + Dye laser (Sirah Credo)	Nd:YAG laser (Edgewave Innoslab)
Detection System	HSS6 (LaVision)	HS IRO + HSS6 (LaVision)	SA-X2 (Photron)
Frequency	1 kHz	10 kHz (real) 1 kHz (effective)	10 kHz
HAB (mm)	0–10	0–24	0–36
Pixel Size (µm)	9.2	32.4	36.8

The ignition process and the volatile-phase flame structure were visualized using planar laser-induced fluorescence (OH-PLIF). A frequency-doubled dye laser system

(Credo, Sirah) incorporating Rhodamine 6G dye and pumped using a diode-pumped solid-state laser (IS8II-E, EdgeWave GmbH, Würselen, Germany) at 532 nm was operated at 10 kHz. The dye laser was tuned by adjusting the resonator grating to 283.01 nm to excite the $Q_1(6)$ transition within the OH A–X(1–0) system, and the wavelength was checked using a wavemeter (WSU-30, HighFinesse GmbH, Tübingen, Germany). The pulse energy was about 0.4 mJ with an approximately 7 ns pulse duration. Spatial scanning of the laser sheet across 10 parallel planes was enabled using an acousto-optical deflector (AOD), providing an effective temporal resolution of 1 kHz. The working principle and the control strategy were initially proposed in [40] and further developed for solid fuel combustion in [41]. Thus, the details are not repeated here for brevity. The scanning OH-LIF technique was utilized to visualize the initiation and evolution of the gas-phase reactions at the particle's center plane. The laser sheet (in $x - y$ plane) spanned approximately 25 mm in height and 130 µm in its full width at half maximum (FWHM), with the scan planes separated by approximately 420 µm, covering a total scanning depth of 3.8 mm. Fluorescence emissions of OH were recorded using a lCMOS camera (HSS6, LaVision GmbH, Göttingen, Germany) in conjunction with a high-speed image intensifier and a UV objective lens (100 mm, CERCO, Saint Martin de Crau, France) , providing a depth of field exceeding 4 mm. A band-pass filter with $\geq$90% transmittance in the 310–320 nm range was employed to suppress flame luminosity and interference from polycyclic aromatic hydrocarbons (PAHs). The OH-PLIF system imaged a region extending up to 24 mm above the burner's surface, with a spatial resolution of 32.4 µm per pixel.

The particle morphology, including size and shape, was characterized using a DBI system operating at 1 kHz with a resolution of 9.2 µm per pixel,which was achieved by coupling the imaging system with a long-distance microscope lens. The particles were back-illuminated using a high-intensity LED source, and shadow images were acquired using a high-speed CMOS camera (HSS6, LaVision GmbH, Göttingen, Germany). The associated magnification led to a restricted field of view (FOV), which was adjusted to span from the burner's exit to approximately 10 mm above the burner's surface.

Particle velocity measurements were conducted via Mie scattering and the particle tracking velocimetry (PTV) technique. The system utilizes a diode-pumped, single-head Nd:YAG laser (Innoslab, EdgeWave GmbH, Würselen, Germany) operating at a wavelength of 532 nm and a pulse repetition rate of 10 kHz with a pulse energy of 2.5 mJ. The laser beam was optically shaped into a slab approximately 8 mm in thickness to increase the probability of interactions of the particles within the sampling volume. Scattered light was detected using a high-speed CMOS camera (SA-X2, Photron, Saugus, MA, USA) coupled with a macro lens, yielding a depth of field exceeding 10 mm. The PTV imaging domain extended approximately 36 mm above the burner's surface, with a projected pixel size of 36.8 µm. The PTV algorithm is described further in Section 2.3.

2.3. Evaluation of Particle Size, Velocity, and Ignition

The initial particle size was determined from DBI measurements using an adaptive thresholding algorithm, which identifies the particle edges based on the local maxima in grayscale gradients. This method, previously validated in [38], has also been applied to extracting particles' non-sphericity and enabling time-resolved measurements of their rotational speed. In the present study, since only the initial particle size and shape were of interest, a single DBI field of view (FOV) was positioned near the burner's surface, as illustrated in Figure 1.

Although DBI provides precise particle positions, the small FOV—chosen to ensure a high spatial resolution—resulted in short observable trajectories. To obtain longer particle tracks and more velocity information, Mie scattering measurements were employed. Owing

to the large FOV of this method, particles can be tracked up to a height above the burner (HAB) of approximately 35 mm, effectively covering most of the volatile combustion phase. Temporal tracking of the particle positions is achieved using blob detection (based on the difference in the Gaussian), followed by Kalman filtering and data association via the Hungarian algorithm, as described in [20]. The results for the particle sizes, shapes, and velocities are presented in Section 3.1.

For high-volatile particles, gas-phase ignition is often associated with weak and noisy OH-LIF signals around the micro-particle, as noted in [20], complicating the accurate determination of the ignition delay due to a poor signal-to-noise ratio (SNR). To mitigate this limitation, multiple detection strategies are applied to extract the ignition timing from the temporal OH-LIF image sequences. A comparative analysis of the ignition delay times obtained from all three detection methods is presented in Section 3.2.

- The first approach identifies ignition based on radial profiles of the OH-LIF intensity (I_{OH}). Figure 2 shows an example for a BC particle at various time steps post-ignition. When a particle intersects with the laser sheet, it appears as a dark stripe, which is excluded from the orientation-averaged intensity calculations. As shown in prior 3D studies [41], I_{OH} increases toward the reaction zone and decreases in the post-flame region. Ignition is defined as the moment when I_{OH} surpasses the normalized background level (unity), attributed to the formation of OH via the dissociation of water in hot gas environments. A rapid rise in I_{OH} is observed within a few milliseconds, followed by a plateau and an eventual decline after 7–8 ms. This behavior reflects the continuous release and consumption of volatiles in a diffusion-controlled, non-premixed flame, where the oxidizer and the fuel meet from opposite directions. The temporal evolution of the radial intensity profile further enables quantification of the flame stand-off distance and the location of the reaction zone, as discussed in Section 3.4.
- The second method employs the structure and signal (SAS) analysis algorithm, which detects the onset of gas-phase reactions by identifying contiguous OH-LIF signal regions. As reported in [19], this technique has proven effective for identifying ignition in particles with diameters near 100 µm.
- The third ignition detection method employs a deep learning approach based on a residual neural network (ResNet) architecture for feature recognition. The implementation details, including the network depth, training data volume, and learning process, are provided in [20]. In this study, a pre-trained ResNet18 model—fine-tuned using planar OH-LIF data from [19]—is used to detect ignition events in the current multi-plane dataset. The advantage of this model is its proven capability to generalize to a new dataset without parameter adjustments, as demonstrated in [20]. The model and training datasets are available on request.

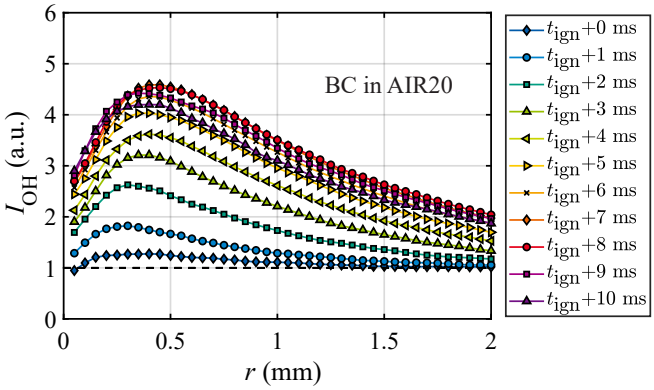


Figure 2. The temporal change in the intensity (I_{OH}) over the radial position (r) of a bituminous coal (BC) particle in AIR20 (N_2/O_2) conditions.

3. Results and Discussion

3.1. The Particle Size Distribution and Velocity Profiles

Particle size is determined by the circle-equivalent particle diameter from the DBI measurements, $d_{prt} = 2\sqrt{A/\pi}$, with A representing the projected particle area. As shown in Figure 3a, both the bituminous coal (BC) and walnut shell (WS) particles exhibit similar size distributions. These particles have an average diameter of approximately 126 µm, with a considerable number of smaller particles (<100 µm) and some larger ones (>150 µm). Compared to BC, the WS particle distribution is slightly broader, extending to sizes approaching 200 µm. Additionally, the d_{prt} distributions are significantly wider than the original sieve range of 106–125 µm and show a noticeable shift toward larger diameters. This behavior is attributed to the non-spherical geometry of the particles. The particles smaller than the sieve's size is probably due to fragmentation during the seeding or combustion process.

Non-sphericity is characterized using the aspect ratio β_{prt}, which is calculated by fitting an ellipse to approximate the particle edge obtained in the DBI measurements. As depicted in Figure 3b, both particle types demonstrate comparable probability density functions for β_{prt}, indicating that most of the particles lie within the range $1 < \beta_{prt} < 2.5$. Such irregular shapes enable particles larger than the nominal sieve cut-off to pass through, leading to the aforementioned broadening and upward shift in the observed size distribution.

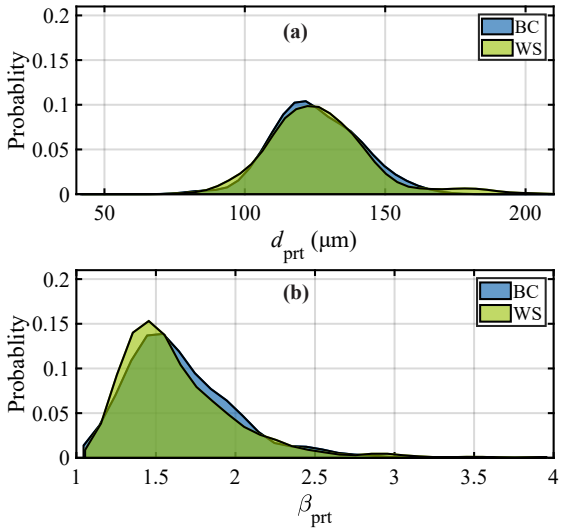


Figure 3. PDFd of the particle diameter (d_{prt}) (**a**) and aspect ratio (β_{prt}) (**b**) of the investigated particles.

It is worth emphasizing that precise particle sizing is essential for accurately determining particles' Reynolds numbers, as the sieve-defined range typically introduces significant uncertainty. Therefore, in situ measurements of particle sizes are crucial for refining the size classification and providing reliable initial conditions in numerical simulations. Furthermore, particles' non-sphericity is often overlooked in numerical models of solid fuel combustion, which can result in substantial rotational dynamics, which in turn may affect the heat transfer and ignition behavior. Incorporating experimentally measured particle shapes has been shown to enhance the fidelity of numerical predictions of ignition delay times [38].

Figure 4 shows the averaged particle velocity profiles at various HABs, with the corresponding gas velocities indicated by dashed lines. The experimental conditions are designed to maintain comparable gas velocities across cases. Specifically, the gas velocity for AIR10–40 conditions is approximately 1.67 m/s, which is higher than the 1.35 m/s measured under OXY20–40 conditions [19]. The gas velocities are shown in dashed lines in Figure 4. Entering the burner, both BC and WS particles accelerate toward the gas's

velocity, generally following an exponential trajectory which agrees well with the previous calculation using Stokes' drag law [38].

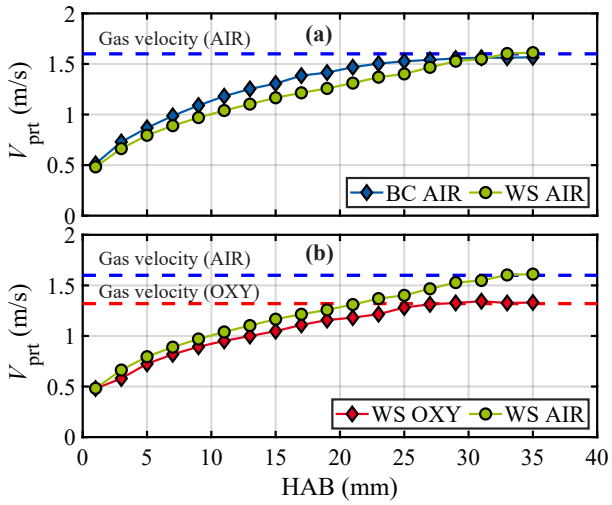


Figure 4. The particle velocities (V_{prt}) over the height above the burner (HAB) of bituminous coal (BC) (**a**) and walnut shell (WS) particles in AIR and OXY conditions (**b**). Dashed lines represent the constant gas velocities.

The particle Reynolds number, denoted as Re_{prt}, is estimated to remain below unity for both particle types. Assuming Stokes' flow, the characteristic particle response time is given by $\tau_{prt} = d_{prt}^2 \rho_{prt}/18\mu$, where ρ_{prt} and μ represent the particle density and the gas's dynamic viscosity, respectively. Figure 4a shows that walnut shell particles exhibit lower velocities than those of coal particles, which is unexpected given their generally lower density (i.e., 800–1000 kg/m^3) compared to that of coal (i.e., about 1200 kg/m^3). Given the accuracy of the velocity measurements, the slower acceleration of the walnut shell particles requires further inspection. One possible explanation could be the slight difference in the particle size, as illustrated in Figure 3a, where the walnut shell particles exhibit a marginally larger peak diameter and a higher fraction near 200 µm. Another plausible hypothesis is that the volatile combustion of walnut shell particles generates a distinct local gas composition and flame temperature, thereby modifying the gas's viscosity in the vicinity of the particle. Additional factors, such as variations in aerodynamic drag due to subtle morphological changes during the early heating phase or differences in radiative properties, may also contribute, although their impact is likely minor. Nevertheless, direct experimental validation of these effects remains challenging, underscoring the need for complementary numerical investigations through CFD simulations in future studies.

3.2. Homogeneous Ignition Delay Times

As explained in Section 2.3, the ignition delay times t_{ign} are determined using three distinct methods: a structure and signal analysis (SAS), a radial intensity analysis (IntR), and a machine-learning-based method (ResNet) previously developed in [20]. Figure 5 presents a comparison of the t_{ign} values for BC and WS particles under various reactor conditions. Overall, the three methods yield consistent ignition delay times, with the discrepancies between the mean t_{ign} (represented by symbols) remaining within the respective standard deviations (represented by error bars). A minor deviation is observed in the SAS results under OXY conditions, likely due to the threshold values being optimized for the signal characteristics in AIR environments. Both the ResNet and IntR methods demonstrate a robust performance with a high computational efficiency. Notably, the ResNet model was trained on another dataset from previous measurements in [20], and its suc-

cessful application here without parameter tuning illustrates its capability to generalize to similar datasets.

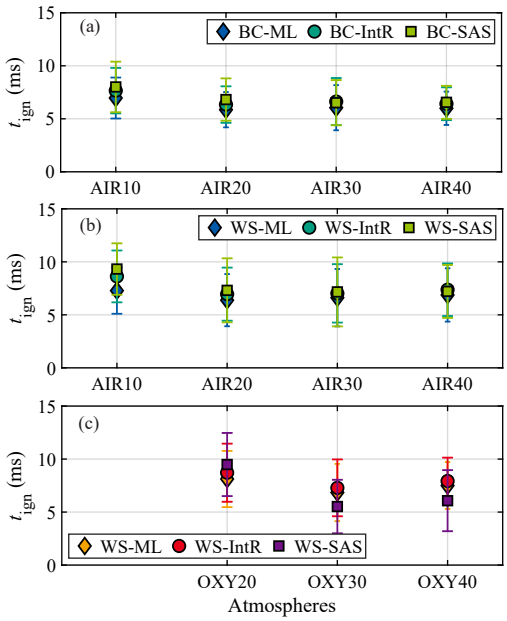


Figure 5. Comparison of ignition delay times (t_{ign}) of bituminous coal (BC) in AIR (N_2/O_2) (**a**), walnut shell (WS) particles in in AIR (N_2/O_2) (**b**) and WS particles in OXY (**c**) atmospheres with increasing oxygen mole fractions. Three detection methods (ResNet, SAS and IntR) are included.

Figure 5 further shows that oxygen enrichment reduces t_{ign}. Ignition is observed to occur earlier as the oxygen mole fraction increases from 10 to 20 vol% in N_2/O_2 and from 20 to 30 vol% in CO_2/O_2 environments. This trend is consistent with previous studies [17,42], which suggest that enhanced oxygen mole fractions accelerate mass diffusion processes, thereby facilitating the formation of a combustible gas mixture. However, with further increases in oxygen mole fraction from 20 to 40 vol% in N_2/O_2 and from 30 to 40 vol% in CO_2/O_2 environments, t_{ign} plateaus, indicating that the ignition process becomes limited by the rate of volatile release rather than by oxygen diffusion.

The volatile release rate is primarily governed by particle temperature, which is influenced by the particle heating rate as the surface oxidation heat is not dominant in homogeneous combustion. Since the gas temperature is maintained constant across all conditions in the established burner [19], comparable heating rates and hence similar volatile release rates can be expected. At lower oxygen levels, ignition is governed by the rate of oxygen diffusion into the volatiles. In contrast, at higher oxygen mole fractions, diffusion occurs faster than volatile release, making the latter the limiting step. It is important to note that the ambient temperature of 1800 K is significantly higher than the auto-ignition temperature of the fuels, ensuring that ignition is not constrained by thermal conditions in this study; however, such constraints may become relevant at lower ambient temperatures.

Another noteworthy observation is that biomass particles do not exhibit shorter ignition delays compared to coal particles. This is counterintuitive, as biomass volatiles are generally considered more reactive due to their higher oxygen content and the presence of smaller molecular species. The comparable t_{ign} values can be explained by the higher moisture content in biomass, which undergoes evaporation during the initial phase of devolatilization. This moisture evaporation retards particle heating and delays volatile gas release [19], thereby offsetting the inherently higher reactivity of biomass.

Furthermore, substituting N_2 with CO_2 as the inert gas does not result in a significant change in the ignition delay for the walnut shell particles. Although CO_2 possesses a

higher heat capacity and is often considered a thermal sink, this effect is negligible in the high-temperature environments studied here. The simulations show that the local gas temperature decreases only slightly during particle heating [19]. Instead, the lower diffusivity of O_2 in CO_2 appears to play a more critical role. The reduction in t_{ign} from OXY20 to OXY30 conditions supports this view, as it suggests that an increasing oxygen partial pressure enhances the O_2 diffusion in a CO_2-rich atmosphere.

3.3. The Temporal and Spatial Evolution of the Volatile Flame Structure

As exemplified in Figure 2, the gas-phase reactions start with ignition and proceed with increasing OH-LIF intensities, peaking around 7 ms in AIR20 before gradually declining. The planar OH-LIF images were time-aligned with the ignition point t_{ign} and subsequently averaged across multiple single-particle events. Typically, more than 100 particles were used for averaging in every condition. Figures 6 and 7 depict the temporal evolution of the planar OH-LIF signals in AIR environments for BC and WS particles, respectively, across increasing oxygen mole fractions X_{O_2}. These sequences confirm the two-dimensional development of the flame dynamics observed earlier in Figure 2. The reaction zone forms a nearly spherical envelope around the particle, with slight downstream elongation due to the slip velocity between the gas and the particle. Obstruction of the laser beam by the particle generates a shadowed region on the left side (the laser direction from right to left).

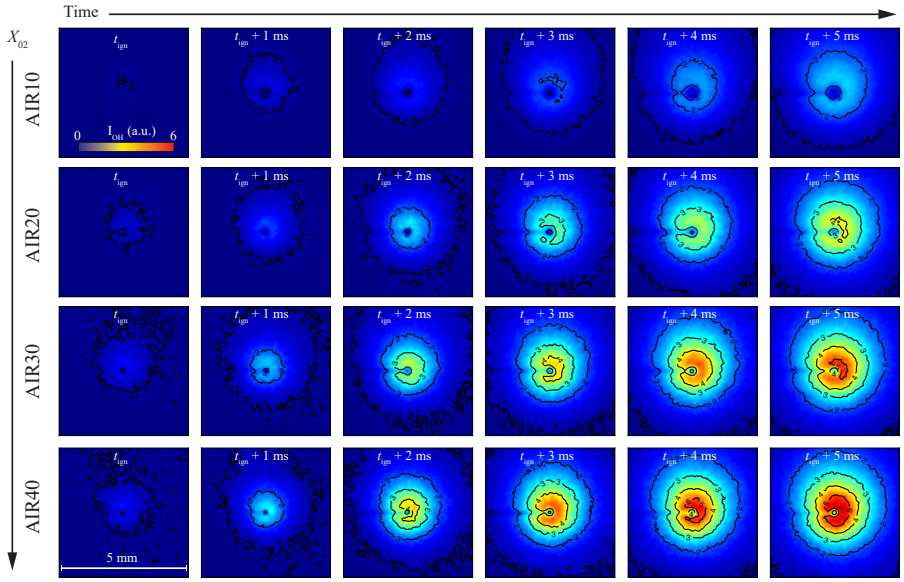


Figure 6. The temporal sequences of the mean OH-LIF intensities (I_{OH}) for bituminous coal (BC) particles starting from the ignition time t_{ign} in AIR10–40.

An increase in X_{O_2} leads to higher OH-LIF intensities at all post-ignition time steps, indicating an enhanced reaction rate within the volatile flame. Due to the non-premixed nature of combustion, the reaction rate is governed by the diffusion rates of the fuel and the oxidizer. Assuming a constant fuel release rate, as discussed previously, higher X_{O_2} promotes faster O_2 diffusion, thereby accelerating fuel consumption. These findings are consistent with earlier studies reporting higher flame or soot temperatures under elevated oxygen mole fractions [17,42–45]. Similarly, Li et al. [19] observed shorter volatile combustion durations with higher X_{O_2}, affirming that the gas-phase reaction rates are strongly coupled with oxygen transport.

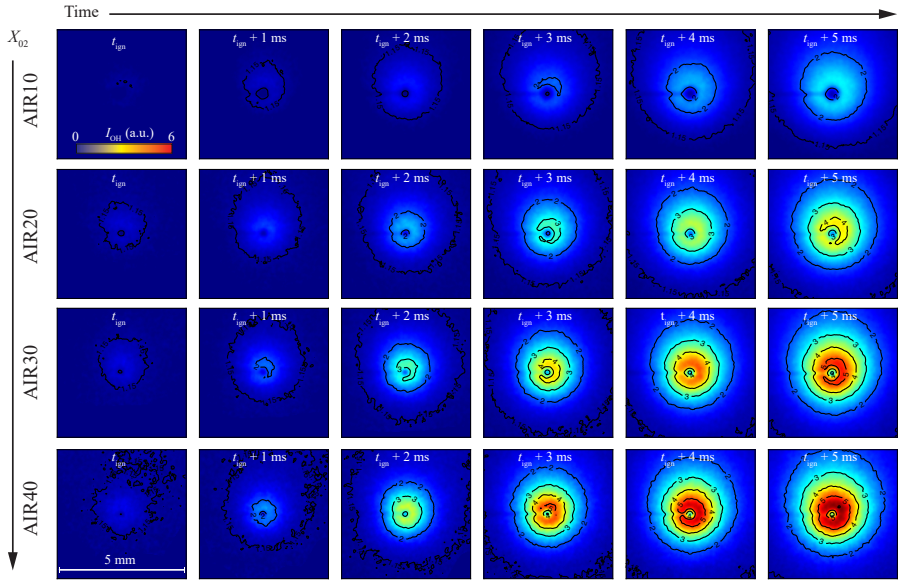


Figure 7. The temporal sequences of the mean OH-LIF intensities (I_{OH}) for walnut shell (WS) particles starting from the ignition time t_{ign} in AIR10–40.

When comparing the flame structures for BC and WS in N_2/O_2 (AIR) conditions, similar features are observed. Although WS contains a higher fraction of reactive volatiles due to bound oxygen groups, a more intense volatile flame is not evident. The comparable flame areas and intensities for BC and WS suggest that the gas-phase reaction behavior is predominantly controlled by oxygen diffusion rather than fuel composition.

A comparable conclusion arises from examining the OH-LIF sequences for the WS particles in CO_2/O_2 (OXY) conditions, as shown in Figure 8. Here, the influence of increasing X_{O_2} (from 20 to 40 vol%) is evident from the intensified OH-LIF signals and expanded flame zones following ignition at t_{ign}. These findings confirm that enhanced oxygen diffusion associated with higher X_{O_2} drives more vigorous volatile combustion.

Comparing the influence of CO_2 and N_2 as the dilatant gases, slightly lower OH-LIF intensities are observed for the WS particles at equivalent X_{O_2} levels in CO_2-containing atmospheres. This reduction in the early-stage flame intensity is attributed to the lower oxygen diffusivity and higher specific heat capacity of CO_2. These observations are consistent with the previously reported longer volatile combustion durations in CO_2 environments [19]. Overall, while the choice of inert gas plays a role, oxygen diffusion remains the dominant factor influencing the gas-phase reactions and flame structure.

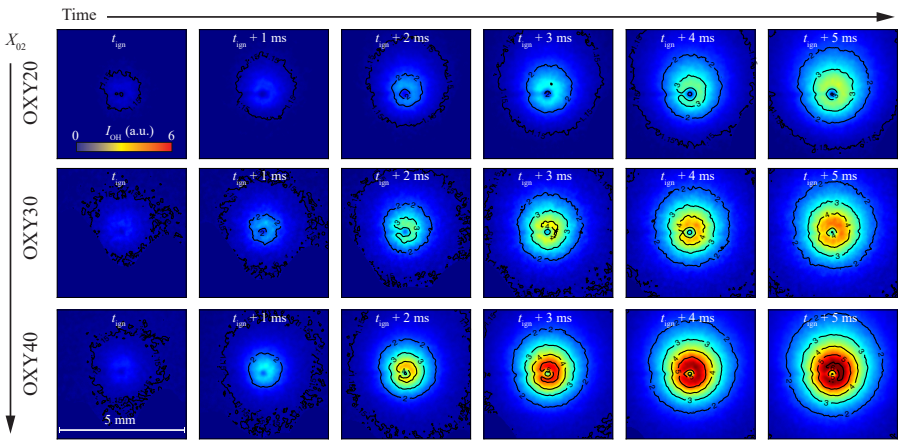


Figure 8. The temporal sequences of the mean OH-LIF intensities (I_{OH}) for walnut shell (WS) particles starting from the ignition time t_{ign} in OXY20–40.

3.4. The Stand-Off Distances of the Volatile Flames

To investigate the temporal evolution of the flame structures further, the flame stand-off distance was evaluated by identifying the location of peak reactivity—defined as the position of the maximum OH-LIF intensity (I_{OH})—and normalizing it by the particle radius, yielding r_{PR}/r_{prt}. The results are presented in Figure 9a–c. Beginning from the ignition point ($\Delta t = 0$ ms), the stand-off distance increases progressively during the early phase of volatile combustion, indicating that the peak reaction zone moves outward from the particles' surface. At higher oxygen mole fractions, however, the volatile flame stabilizes closer to the particles, which can be attributed to the enhanced oxygen diffusion facilitated by elevated far-field X_{O_2}.

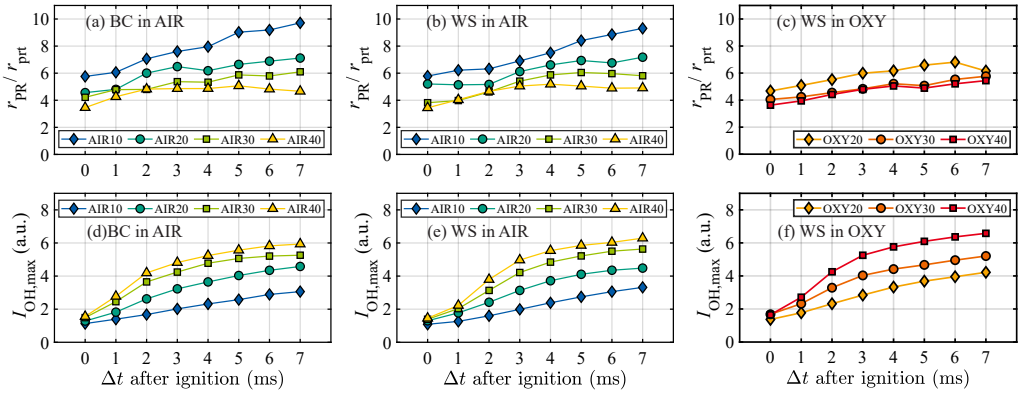


Figure 9. The normalized flame stand-off distance (r_{PR}/r_{prt}) and maximum OH-LIF intensity ($I_{OH,max}$) of bituminous coal (BC) and walnut shell (WS) particles in various AIR and OXY atmospheres.

For WS particles, the flame stand-off distance remains nearly constant when X_{O_2} is unchanged, indicating the steady positioning of the peak reaction zone under fixed oxidizer conditions. Additionally, the maximum OH-LIF intensity ($I_{OH,max}$), representing the peak reactivity, is shown in Figure 9d–f. Across different fuel types and inert gas environments, the early-stage volatile flame consistently exhibits a growing trend in both its size and intensity. This quantitative assessment complements the observations of the 2D flame structure discussed in Section 3.3, reinforcing the conclusion that oxygen diffusion to the particles' surface is the rate-limiting step during the early volatile combustion phase. Overall, the homogeneous combustion of single coal and biomass particles examined in this study clearly exhibits non-premixed flame characteristics.

4. Conclusions

This study extends our ongoing investigation of single-particle combustion in high-temperature environments using advanced multi-parameter optical diagnostics. The primary objective is to elucidate the ignition behavior and early-stage evolution of volatile flames from biomass and coal particles, with a particular focus on the influence of the oxidizer and inert gas composition. To this end, volatile flames from individual walnut shell particles are examined using synchronized high-speed DBI, Mie scattering, and OH-LIF measurements. This multi-parameter optical diagnostic approach enables a better statistical analysis conditioned on the particle size and ignition initiation, reducing the uncertainties in the experimental data. Leveraging the particle morphology and velocity determined in situ, the effects of the gas composition on the ignition and flame characteristics are systematically evaluated.

For particles with an average diameter of 126 µm, the ignition delay times are observed to decrease with an increasing oxygen mole fraction (X_{O_2}) up to 20–30 vol% but plateau

at 40 vol%. This trend indicates that at elevated oxygen levels, the rate of volatile release becomes the dominant factor limiting ignition. In both CO_2/O_2 and N_2/O_2 atmospheres, the development of the volatile flame accelerates with increasing X_{O_2}, as evidenced by the greater flame stand-off distances and enhanced OH-LIF intensities. These observations emphasize the non-premixed combustion behavior of the volatile matter, where the diffusion of oxygen toward the particles' surface is the primary controlling mechanism.

Furthermore, substituting N_2 with CO_2 under constant X_{O_2} does not significantly alter the ignition delay or the early flame dynamics, suggesting that the type of inert gas exerts a minimal influence under these conditions. Additionally, under identical atmospheres, walnut shell and high-volatile bituminous coal particles exhibit comparable ignition delay times and volatile flame structures. The findings from these fundamental experiments provide a valuable dataset for model validation and offer physical insights into high-volatile particle combustion, supporting future scale-up studies and the development of cleaner electricity generation technologies.

Author Contributions: Conceptualization, T.L.; Methodology, T.L.; Software, H.C.; Formal analysis, H.C.; Investigation, T.L.; Data curation, T.L.; Writing—original draft, T.L.; Writing—review & editing, H.C. and B.B.; Supervision, B.B.; Project administration, B.B.; Funding acquisition, B.B. All authors have read and agreed to the published version of the manuscript.

Funding: The author kindly acknowledges the financial support from Deutsche Forschungsgemeinschaft (DFG)—Projektnummer 215035359—TRR 129 through CRC/Transregio 129 "Oxy-flame: Development of Methods and Models to Describe Solid Fuel Reactions Within an Oxy-Fuel Atmosphere".

Data Availability Statement: The original contributions presented in this study are included in the article. Further inquiries can be directed to the corresponding author.

Acknowledgments: This article is a revised and expanded version of a paper entitled "Assessing the Gas Composition Effects on Volatile Flames of Solid Fuels Using Multi-Parameter Optical Diagnostics", which has been presented at the 13th Mediterranean Combustion Symposium, Corfu, Greece, on 1–6 June 2025.

Conflicts of Interest: The author declares no conflicts of interest.

References

1. Toftegaard, M.B.; Brix, J.; Jensen, P.A.; Glarborg, P.; Jensen, A.D. Oxy-fuel combustion of solid fuels. *Prog. Energy Combust. Sci.* **2010**, *36*, 581–625. [CrossRef]
2. Williams, A.; Pourkashanian, M.; Jones, J.M. Combustion of pulverised coal and biomass. *Prog. Energy Combust. Sci.* **2001**, *27*, 587–610. [CrossRef]
3. Hupa, M.; Karlström, O.; Vainio, E. Biomass combustion technology development—It is all about chemical details. *Proc. Combust. Inst.* **2017**, *36*, 113–134. [CrossRef]
4. Li, S.; Xu, Y.; Gao, Q. Measurements and modelling of oxy-fuel coal combustion. *Proc. Combust. Inst.* **2019**, *37*, 2643–2661. [CrossRef]
5. Hasse, C.; Debiagi, P.; Wen, X.; Hildebrandt, K.; Vascellari, M.; Faravelli, T. Advanced modeling approaches for CFD simulations of coal combustion and gasification. *Prog. Energy Combust. Sci.* **2021**, *86*, 100938. [CrossRef]
6. Li, T.; Geschwindner, C.; Dreizler, A.; Böhm, B. Particle-resolved optical diagnostics of solid fuel combustion for clean power generation: A review. *Meas. Sci. Technol.* **2023**, *34*, 122001. [CrossRef]
7. Buhre, B.; Elliott, L.K.; Sheng, C.D.; Gupta, R.P.; Wall, T.F. Oxy-fuel combustion technology for coal-fired power generation. *Prog. Energy Combust. Sci.* **2005**, *31*, 283–307. [CrossRef]
8. Wall, T.; Liu, Y.; Spero, C.; Elliott, L.; Khare, S.; Rathnam, R.; Zeenathal, F.; Moghtaderi, B.; Buhre, B.; Sheng, C.; et al. An overview on oxyfuel coal combustion—State of the art research and technology development. *Chem. Eng. Res. Des.* **2009**, *87*, 1003–1016. [CrossRef]
9. Scheffknecht, G.; Al-Makhadmeh, L.; Schnell, U.; Maier, J. Oxy-fuel coal combustion—A review of the current state-of-the-art. *Int. J. Greenh. Gas Control* **2011**, *5*, S16–S35. [CrossRef]

10. Chen, L.; Yong, S.Z.; Ghoniem, A.F. Oxy-fuel combustion of pulverized coal: Characterization, fundamentals, stabilization and CFD modeling. *Prog. Energy Combust. Sci.* **2012**, *38*, 156–214. [CrossRef]
11. Tillman, D. Biomass cofiring: The technology, the experience, the combustion consequences. *Biomass Bioenergy* **2000**, *19*, 365–384. [CrossRef]
12. Demirbas, A. Combustion characteristics of different biomass fuels. *Prog. Energy Combust. Sci.* **2004**, *30*, 219–230. [CrossRef]
13. Williams, A.; Jones, J.M.; Ma, L.; Pourkashanian, M. Pollutants from the combustion of solid biomass fuels. *Prog. Energy Combust. Sci.* **2012**, *38*, 113–137. [CrossRef]
14. Köser, J.C. Untersuchung der frühen Abbrandphase von Feststoffpartikeln mit optischer Diagnostik. Ph.D. Thesis, Technische Universität Darmstadt, Darmstadt, Germany, 2020. [CrossRef]
15. MoliMolina, A.; Shaddix, C.R. Ignition and devolatilization of pulverized bituminous coal particles during oxygen/carbon dioxide coal combustion. *Proc. Combust. Inst.* **2007**, *31*, 1905–1912. [CrossRef]
16. Yuan, Y.; Li, S.; Xu, Y.; Yao, Q. Experimental and theoretical analyses on ignition and surface temperature of dispersed coal particles in O_2/N_2 and O_2/CO_2 ambients. *Fuel* **2017**, *201*, 93–98. [CrossRef]
17. Shaddix, C.R.; Molina, A. Particle imaging of ignition and devolatilization of pulverized coal during oxy-fuel combustion. *Proc. Combust. Inst.* **2009**, *32*, 2091–2098. [CrossRef]
18. Li, L.; Duan, L.; Zeng, D.; Lu, D.Y.; Bu, C.; Zhao, C. Ignition and volatile combustion behaviors of a single lignite particle in a fluidized bed under O_2/H_2O condition. *Proc. Combust. Inst.* **2019** , *37*, 4451–4459. [CrossRef]
19. Li, T.; Farmand, P.; Geschwindner, C.; Greifenstein, M.; Köser, J.; Schumann, C.; Attili, A.; Pitsch, H.; Dreizler, A.; Böhm, B. Homogeneous ignition and volatile combustion of single solid fuel particles in air and oxy-fuel conditions. *Fuel* **2021**, *291*, 120101. [CrossRef]
20. Li, T.; Liang, Z.; Dreizler, A.; Böhm, B. Accurate determination of homogeneous ignition of single solid fuel particles enabled by machine learning. *Fuel* **2023**, *338*, 127171. [CrossRef]
21. Ma, P.; Huang, Q.; Wu, Z.; Lyu, J.; Li, S. Optical diagnostics on coal ignition and gas-phase combustion in co-firing ammonia with pulverized coal on a two-stage flat flame burner. *Proc. Combust. Inst.* **2023**, *39*, 3457–3466. [CrossRef]
22. Bejarano, P.A.; Levendis, Y.A. Single-coal-particle combustion in O_2/N_2 and O_2/CO_2 environments. *Combust. Flame* **2008**, *153*, 270–287. [CrossRef]
23. Mock, C.; Lee, H.; Choi, S.; Manovic, V. Combustion Behavior of Relatively Large Pulverized Biomass Particles at Rapid Heating Rates. *Energy Fuels* **2016**, *30*, 10809–10822. [CrossRef]
24. Chen, H.; Abdallah, M.; Dreizler, A.; Böhm, B.; Li, T. Simultaneous LII, PAH-LIF, OH-LIF, and Mie scattering measurements in solid fuel particle combustion. *Proc. Combust. Inst.* **2024**, *40*, 105711. [CrossRef]
25. Lee, H.; Choi, S. An observation of combustion behavior of a single coal particle entrained into hot gas flow. *Combust. Flame* **2015**, *162*, 2610–2620. [CrossRef]
26. Zhang, D.; Wall, T. Ignition of coal particles: The influence of experimental technique. *Fuel* **1994**, *73*, 1114–1119. [CrossRef]
27. Levendis, Y.A.; Joshi, K.; Khatami, R.; Sarofim, A.F. Combustion behavior in air of single particles from three different coal ranks and from sugarcane bagasse. *Combust. Flame* **2011**, *158*, 452–465. [CrossRef]
28. Khatami, R.; Stivers, C.; Joshi, K.; Levendis, Y.A.; Sarofim, A.F. Combustion behavior of single particles from three different coal ranks and from sugar cane bagasse in O_2/N_2 and O_2/CO_2 atmospheres). *Combust. Flame* **2012**, *159*, 1253–1271. [CrossRef]
29. Mock, C.; Lee, H.; Choi, S.; Manovic, V. Flame structures and ignition characteristics of torrefied and raw sewage sludge particles at rapid heating rates. *Fuel* **2017**, *200*, 467–480. [CrossRef]
30. Simões, G.; Magalhães, D.; Rabaçal, M.; Costa, M. Effect of gas temperature and oxygen concentration on single particle ignition behavior of biomass fuels. *Proc. Combust. Inst.* **2017**, *36*, 2235–2242. [CrossRef]
31. Panahi, A.; Vorobiev, N.; Schiemann, M.; Tarakcioglu, M.; Delichatsios, M.; Levendis, Y.A. Combustion details of raw and torrefied biomass fuel particles with individually-observed size, shape and mass. *Combust. Flame* **2019**, *207*, 327–341. [CrossRef]
32. Lei, K.; Ye, B.; Cao, J.; Zhang, R.; Liu, D. Combustion Characteristics of Single Particles from Bituminous Coal and Pine Sawdust in O_2/N_2, O_2/CO_2, and O_2/H_2O Atmospheres. *Energies* **2017**, *10*, 1695. [CrossRef]
33. Riaza, J.; Khatami, R.; Levendis, Y.A.; Álvarez, L.; Gil, M.V.; Pevida, C.; Rubiera, F.; Pis, J.J. Combustion of single biomass particles in air and in oxy-fuel conditions. *Biomass Bioenergy* **2014**, *64*, 162–174. [CrossRef]
34. Li, T.; Farmand, P.; Chen, H.; Boehme, C.; Nicolai, H.; Hasse, C.; Pitsch, H.; Böhm, B. Homogeneous ignition and volatile flame structure of single bituminous coal and walnut shell particles: Effects of particle size and gas atmosphere. *Fuel* **2024**, *371*, 131955. [CrossRef]
35. Farazi, S.; Hinrichs, J.; Davidovic, M.; Falkenstein, T.; Bode, M.; Kang, S.; Attili, A.; Pitsch, H. Numerical investigation of coal particle stream ignition in oxy-atmosphere. *Fuel* **2019**, *241*, 477–487. [CrossRef]
36. Tufano, G.L.; Stein, O.T.; Kronenburg, A.; Frassoldati, A.; Faravelli, T.; Deng, L.; Kempf, A.M.; Vascellari, M.; Hasse, C. Resolved flow simulation of pulverized coal particle devolatilization and ignition in air- and O_2/CO_2 -atmospheres. *Fuel* **2016**, *186*, 285–292. [CrossRef]

37. Goshayeshi, B.; Sutherland, J.C. A comparison of various models in predicting ignition delay in single-particle coal combustion. *Combust. Flame* **2014**, *161*, 1900–1910. [CrossRef]
38. Li, T.; Li, B.; Farmand, P.; Dreizler, A.; Pitsch, H.; Böhm, B. Motion and swelling of single coal particles during volatile combustion in a laminar flow reactor. *Proc. Combust. Inst.* **2023**, *39*, 3333–3341. [CrossRef]
39. Li, T.; Geschwindner, C.; Dreizler, A.; Böhm, B. An experimental study of coal particle group combustion in conventional and oxy-fuel atmospheres using multi-parameter optical diagnostics. *Proc. Combust. Inst.* **2023**, *39*, 3259–3269. [CrossRef]
40. Li, T.; Pareja, J.; Becker, L.; Heddrich, W.; Dreizler, A.; Böhm, B. Quasi-4D laser diagnostics using an acousto-optic deflector scanning system. *Appl. Phys. B* **2017**, *123*, 78 . [CrossRef]
41. Li, T.; Schiemann, M.; Köser, J.; Dreizler, A.; Böhm, B. Experimental investigations of single particle and particle group combustion in a laminar flow reactor using simultaneous volumetric OH-LIF imaging and diffuse backlight-illumination. *Renew. Sustain. Energy Rev.* **2021**, *136*, 110377. [CrossRef]
42. Riaza, J.; Khatami, R.; Levendis, Y.A.; Álvarez, L.; Gil, M.V.; Pevida, C.; Rubiera, F.; Pis, J.J. Single particle ignition and combustion of anthracite, semi-anthracite and bituminous coals in air and simulated oxy-fuel conditions. *Combust. Flame* **2014**, *161*, 1096–1108. [CrossRef]
43. Schiemann, M.; Scherer, V.; Wirtz, S. Optical Coal Particle Temperature Measurement under Oxy-Fuel Conditions: Measurement Methodology and Initial Results. *Chem. Eng. Technol.* **2009**, *32*, 2000–2004. [CrossRef]
44. Maffei, T.; Khatami, R.; Pierucci, S.; Faravelli, T.; Ranzi, E.; Levendis, Y.A. Experimental and modeling study of single coal particle combustion in O_2/N_2 and Oxy-fuel O_2/CO_2 atmospheres. *Combust. Flame* **2013**, *160*, 2559–2572. [CrossRef]
45. Khatami, R.; Levendis, Y.A.; Delichatsios, M.A. Soot loading, temperature and size of single coal particle envelope flames in conventional- and oxy-combustion conditions (O_2/N_2 and O_2 $/CO_2$). *Combust. Flame* **2015**, *162*, 2508–2517. [CrossRef]

Disclaimer/Publisher's Note: The statements, opinions and data contained in all publications are solely those of the individual author(s) and contributor(s) and not of MDPI and/or the editor(s). MDPI and/or the editor(s) disclaim responsibility for any injury to people or property resulting from any ideas, methods, instructions or products referred to in the content.